Constitutive Behavior of an AA4032 Piston Alloy with Cu and Er Additions upon High-Temperature Compressive Deformation

SUWAREE CHANKITMUNKONG, DMITRY G. ESKIN, and CHAOWALIT LIMMANEEVICHITR

Aluminum piston alloys of the AA4032 type are produced by direct-chill (DC) casting and subsequent forging; therefore, it is important to understand their thermomechanical behavior. In recent years, it was shown that additions of Cu and Er could improve mechanical properties of these alloys at room and high temperatures. In this work, we studied the constitutive behavior of AA4032-type alloys with and without Cu and Er additions. The experimental true stress–true strain curves were obtained by compression tests under various temperatures [683 K to 723 K (410 °C to 450 °C)] and strain rates (0.01 to 10 s^{-1}) to determine constitutive parameters [strain-rate sensitivity, activation energy, and Zener–Hollomon (Z) parameter] for the hot deformation behavior of AA4032-type piston alloys with and without additions of Cu and Er. The flow stress decreased with increasing deformation temperature and decreasing strain rate. The results also showed that increasing the Cu content increased the flow stress over the applied range of deformation conditions due to solid-solution strengthening and the formation of primary Si particles, which led to an increase in the activation energy during hot deformation. Moreover, the main microstructural damage in the AA4032 alloy with 3.5 pct Cu was predominantly due to the cracking of primary Si particles. Additions of 0.4 pct Er and 3.5 pct Cu lower the activation energy of deformation, Q, as compared to the base alloy and the alloy with 3.5 pct Cu. The microstructures in the deformed specimens consisted of subgrains, recrystallized grains, and fine eutectic phases. The alloys containing Er demonstrated more polygonized grains at a low strain rate than the alloys without Er, indicating that Er hindered recrystallization development. The peak stress of the AA4032 alloy with 3.5 pct Cu alloy was higher than for the base AA4032 alloy and for the AA4032 alloy with 3.5 pct Cu and 0.4 pct Er additions, which was attributed to the prevalence of the work-hardening mechanism over the softening mechanism.

https://doi.org/10.1007/s11661-019-05482-9

I. INTRODUCTION

ALUMINUM alloys are widely used in the automotive industry where light weight becomes important due to the introduction of electric vehicles and the needed reduction of emissions. For internal combustion engines, aluminum piston alloys are often used in engine parts that are exposed to high temperatures. Pistons are mainly manufactured by either casting or forging. Though similar in composition to casting piston alloys, wrought piston alloys require a different set of properties. In particular, the thermomechanical behavior of these alloys upon deformation becomes critical. However, there are limited reference data on the constitutive parameters that describe the thermomechanical behavior of high-silicon (near-eutectic) alloys. These constitutive parameters are important for computer simulations of alloy processing, which is useful for designing metal-forming processes, and consequently for obtaining high-quality final products. There are two main mechanisms that occur in the microstructure during hot deformation. The first mechanism is work hardening, which results from dislocation generation and hindered

SUWAREE CHANKITMUNKONG is with the Department of Production Engineering, Faculty of Engineering, King Mongkut's University of Technology Thonburi, 126 Pracha-Utid Rd., Bangmod, Tungkhru, Bangkok 10140 Thailand, and Brunel University London, BCAST, Uxbridge, Middlesex UB8 3PH, UK. Contact email: suwaree.03@mail.kmutt.ac.th DMITRY G. ESKIN is with the Brunel University London, BCAST, and the Tomsk State University, Tomsk, Russian Federation 634050. CHAOWALIT LIMMANEEVICHITR is with the Department of Production Engineering, Faculty of Engineering, King Mongkut's University of Technology Thonburi.

Manuscript submitted May 5, 2019.

Published online: 25 October 2019

movement in the structure. The increase of dislocation density and misorientation of grains during deformation results in the increase of the flow stress and strain hardening.[1] The second mechanism is softening, which includes dynamic recovery (DRV) and dynamic recrystallization (DRX), or static recrystallization after the end of hot deformation.[2] These mechanisms can be related to the activation energy of deformation and the Zener–Hollomon (Z) parameter.[3] Recently, the electron backscattered diffraction (EBSD) technique was successfully used to analyze the recrystallization phenomena because it could show the grain orientations in relation to the neighboring grains after hot deformation.[4,5]

Workability is usually defined as the amount of deformation and level of ductility that enables material plastic deformation without fracture or cracking, reaching desirable deformed microstructures at a given temperature and strain rate.[2] Improving workability means increasing the processing ability and improving the properties of the materials. This could be achieved by optimizing the deformation temperature and strain rate in hot processing. The deformation behavior of an AA4032 alloy was previously studied from 653 K to 753 K (380 °C to 480 °C) in a wide strain-rate range from 0.01 to 10 s^{-1} in order to optimize for the hot working operation (*i.e.*, hot forging process). It was found that the solute elements, such as Mg and Si, can cause the increase in the activation energy for hot deformation.[6] In related works, it is shown that the addition of alloying elements (*i.e.*, Mn and Cr[7] or Cu[8,9]) can increase the complexity of the precipitation sequence during age hardening, which may compromise the hot workability characteristics of the alloy. The mechanical properties of this type of alloy can be significantly improved at elevated temperatures by Er alloying,[10] which was mainly attributed to the presence of Al_3Er particles.[10–12] However, the effects of combined Cu and Er additions on the constitutive parameters and flow behavior of this type of alloy, which includes the constitutive behavior, as well as the work-hardening and softening mechanisms during hot deformation, have not yet been studied. In order to predict the material flow behavior under specific conditions in hot working, constitutive equations are used to describe the flow stress and optimum parameters that can facilitate reliable simulation results of deformation processes.[13] Various models have been developed and used to predict the constitutive behavior of aluminum alloys upon hot deformation, such as the Johnson–Cook and Arrhenius models.[14] In recent years, the strain-compensated Arrhenius model was successfully applied to predict the flow behavior of aluminum alloys at elevated temperature.[15]

Aluminum piston alloys are complex in chemical and phase compositions. The alloying elements play a decisive role in the mechanical behavior of the alloys through the formation of phases and by affecting the microstructure. In this article, we study the effects of Cu and Er additions on hot deformation behavior. It was recently shown that a high Cu addition to an AA4032 alloy promoted the formation of primary Si particles through the shift of the eutectic point in the system, while the addition of Er significantly decreased the amount of primary Si and resulted in overall structural refinement.[10] A combined addition of Cu and Er increased the thermal stability of an as-cast alloy at temperatures above 573 K (300 °C) through the formation of temperature-resistant phases and structure refinement.[10,11] Moreover, it was reported that the addition of Er to an Al-Si alloy could form precipitates of the Al_3Er phase, which improved high-temperature strength.[11] Furthermore, it was reported that the deformation behavior of Al-Si based as-cast alloys was related to microstructural changes associated with the secondary phases, precipitates, and morphology of eutectic phases.[16,17] Therefore, we need to take into account that the addition of alloying elements to Al-Si alloys can enhance the strength of these alloys but at the same time may affect their hot workability.

In this article, we consider a forgeable 4XXX series alloy that is typically produced by direct-chill (DC) casting and then forged into the final product, *i.e.*, piston. We studied the thermomechanical behavior of as-cast AA4032 alloys and the effects of Cu and Er additions on this deformation behavior. The study was carried out through extraction of the constitutive parameters based on the Arrhenius model and Z parameter from the flow curves of compression testing in a range of temperatures and strain rates. The results were also supported by microstructural analysis. We analyzed the constitutive parameters and related them to the microstructural evolution under different conditions of the deformation.

II. METHODOLOGY

A. *Materials and Experimental Procedure*

To study the microstructural and mechanical properties of AA4032 billets, the experimental alloys were prepared using high-purity Al ingot (99.9 wt pct), commercial purity crystalline Si (99.9 wt pct), pure Cu (99.9 wt pct), pure Mg (99.5 wt pct), and Al-20 wt pct Ni, Al-10 wt pct Fe, and Al-10 wt pct Er master alloys. The 60-mm-diameter billets were made by DC casting. The alloys were melted in a silicon carbide crucible using a 12-kW induction furnace, and then the melt was continuously poured at a temperature of 993 K (720 °C) into a hot top water-cooled mold. The bottom block was withdrawn downward at a casting speed of 190 mm/min. The chemical composition of the billets was analyzed by emission spectrometry, and the results are given in Table I. The chemical compositions of the billets studied in this work were selected because our previous study[10] showed that the optimum mechanical properties were obtained at these specific amounts of additions.

Samples for mechanical testing were taken from the billets at the midradius position and machined into a cylindrical shape 5 mm in diameter and 10 mm in length. Three samples were tested for each combination of temperature and strain rate to study the statistical behavior. Figure 1 shows the cycle of the hot

Table I. Average Chemical Compositions of AA4032-Type Cast Aluminum Alloys with Various Contents of Cu and Er

	Elements (Wt Pct)						
Alloys	Si	Cu	Mg	Ni	Fe	Er	Al
1Cu (Base Alloy)	12.89	1.15	0.72	0.94	0.60	—	bal
3.5Cu	12.83	3.51	0.69	0.91	0.52	—	bal
3.5Cu + 0.4Er	12.95	3.57	0.72	0.91	0.53	0.4	bal

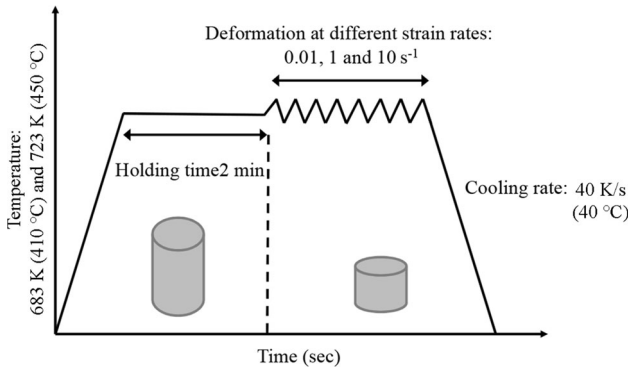

Fig. 1—Schematic diagram of the time-temperature compressive test cycle showing the range of process parameters.

deformation test to determine the stress-strain behavior of the experimental alloys. The hot compression tests were performed using a quench-deformation dilatometer DIL 805A/D. The samples were deformed under hot compression at either 683 K or 723 K (410 °C or 450 °C) with strain rates of 0.01, 0.1, or 10 s^{-1}. A thermocouple was welded on the specimen to monitor and measure the temperatures during the entire heating, deformation, and quenching cycle. The testing cycle can be described as follows: a sample was initially fixed in the chamber and heated to the deformation temperature at a heating rate of 10 K/s (10 °C/s), held for 2 minutes, and subsequently compressed at a prescribed strain rate. Finally, it was quenched with argon gas. True stress–true strain curves were automatically recorded during the entire test cycle. The constitutive parameters were extracted using a combination of Arrhenius equations and Z parameters,[2,18] as described in Section II–B.

Thermo-Calc software with a TCAL4 database was used for calculating the chemical composition of the aluminum solid solution at 803 K (530 °C) (at the end of solidification) and the precipitated phases at 683 K to 723 K (410 °C to 450 °C) (in the range of hot deformation).

The as-cast and deformed samples were analyzed using an optical microscope (Zeiss Axio Scope.A1) and scanning electron microscope (SEM) with a field emission electron gun (Zeiss Supra 55-VP). The deformed samples were sliced parallel to the compression axis in the centerline plane. They were then polished and etched with Keller's reagent. The EBSD technique was used to determine the misorientation of subgrains in deformed samples. The step size between the scanning points' EBSD was set as 0.3 μm. The average misorientation values were based on the analysis of at least five subgrains using the OIM TSL Software 7 (EDAX Ametek). The boundaries of subgrains were defined as low-angle grain boundaries (LAGBs) or high-angle grain boundaries (HAGBs) when misorientation angles were less than 5 deg or greater than 15 deg, respectively.[19]

B. *Constitutive Equations*

1. *Constitutive equations for material constants and Z parameters*

Flow stress curves obtained from the compression tests under different strain rates and temperatures can be used to determine the material constants of the constitutive equations. It is known that there are different constitutive models proposed to describe the flow behavior and determine the material constants during hot deformation, including the activation energy and strain-rate sensitivity. The Arrhenius equations are usually used to accurately describe the relationship between the strain rate, deformation temperatures, and flow stress as follows[20,21]:

$$\dot{\varepsilon} = A_1 \sigma^{n'} \exp\left(-\frac{Q}{RT}\right) \quad [1]$$

$$\dot{\varepsilon} = A_2 \exp(\beta\sigma) \exp\left(-\frac{Q}{RT}\right) \quad [2]$$

$$\dot{\varepsilon} = A_3 [\sinh(\alpha\sigma)]^n \exp\left(-\frac{Q}{RT}\right) \quad [3]$$

Here, $\dot{\varepsilon}$ is the strain rate (s^{-1}); T is the absolute temperature (Kelvin); R is the gas constant (8.314 J/mol K); Q is the hot deformation activation energy (kJ/mol); σ is the flow stress (MPa) for a given strain; and A_1, A_2, A_3, n', n, β, and α are the material constants, where α is defined as $\alpha = \beta/n'$. The power law of Eq. [1] is used at a low stress level when $\alpha\sigma < 0.8$; the exponential law of Eq. [2] is suitable for high stress levels when $\alpha\sigma > 1.2$. The hyperbolic sine law of Eq. [3] can describe the relationship between the deformation parameters for the entire range of stresses (including low and high stress levels).[1,22–24] This constitutive model represents a plasticity model.[25] Therefore, the constitutive parameters extracted in this work were only taken for the stress-strain curves beyond the elastic part. By taking the logarithm of both sides of Eqs. [1] through [3], we obtain

$$\ln \dot{\varepsilon} = \ln A_1 - \frac{Q}{RT} + n' \ln \sigma \quad [4]$$

$$\ln \dot{\varepsilon} = \ln A_2 - \frac{Q}{RT} + \beta\sigma \quad [5]$$

$$\ln \dot{\varepsilon} = \ln A_3 + n \ln[\sinh(\alpha\sigma)] - \frac{Q}{RT} \quad [6]$$

According to Eqs. [4] and [5], the relationship plots of $\ln\sigma - \ln \dot{\varepsilon}$ and $\sigma - \ln \dot{\varepsilon}$ can be used to obtain the values of n' and β, respectively. These relationships can be plotted by a group of parallel and straight lines, and the slopes of these lines approximately remain constant; thus, the values of n' and β can be obtained from the slopes of the lines by the linear fitting method under different deformation temperatures. These are illustrated in Figures 2(a) and (b) for the peak flow stress (Figures 4(a) and 5(a)).

The hot deformation activation energy is an important physical parameter serving as an indicator of the deformation difficulty in plasticity deformation. In order to estimate the activation energy Q of the hot deformation, differentiating Eq. [6] for a given strain rate gives

$$Q = R\left[\frac{\partial \ln \dot{\varepsilon}}{\partial \ln[\sinh(\alpha\sigma)]}\right]_T \left[\frac{\partial \ln[\sinh(\alpha\sigma)}{\partial\left(\frac{1}{T}\right)}\right]_{\dot{\varepsilon}} = Rns \quad [7]$$

According to Eq. [7], n is the slope of $\ln \dot{\varepsilon} - \ln[\sinh(\alpha\sigma)]$ (Figure 2(c)) at different temperatures and s is the slope of $\ln[\sinh(\alpha\sigma)] - 1/T$ (Figure 2(d)). The values of n and s are determined by calculating the average slopes of these relationships.[26]

The Z parameter can be used to characterize the combined effects of strain rate and temperature on the deformation behavior and is mathematically expressed as Eq. [8][1,27] by using the expression of the hyperbolic sine function from Eq. [3]:

$$Z = \dot{\varepsilon} \exp\left(\frac{Q}{RT}\right) = A_3[\sinh(\alpha\sigma)]^n \quad [8]$$

By solving Eq. [8] using the definition of the hyperbolic sine function, the flow stress can be described by the Z parameter as

$$\sigma = \frac{1}{\alpha} \ln\left\{\left(\frac{Z}{A_3}\right)^{1/n} + \left[\left(\frac{Z}{A_3}\right)^{2/n} + 1\right]^{1/2}\right\} \quad [9]$$

The $\ln Z$ values of the deformed samples under different deformation conditions can be obtained from Eq. [9]. The value of $\ln A_3$ can be obtained from the intercept of the $\ln Z - \ln[\sinh(\alpha\sigma)]$ curve, as shown in Figure 3.

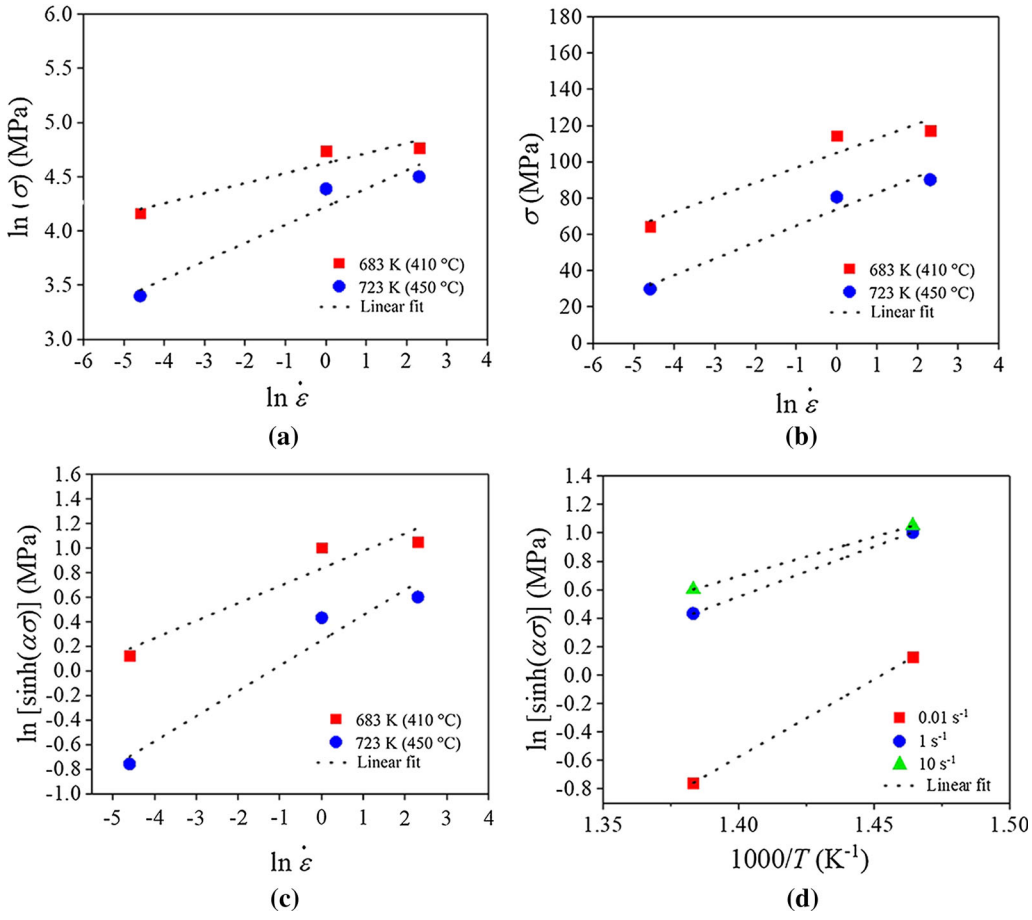

Fig. 2—Relationship plots between (*a*) $\ln \sigma_p - \ln \dot{\varepsilon}$, (*b*) $\sigma_p - \ln \dot{\varepsilon}$, (*c*) $\ln\dot{\varepsilon} - \ln[\sinh(\alpha\sigma)]$, and (*d*) $\ln[\sinh(\alpha\sigma)] - 1/T$ for the base alloy at the peak stress (Figs. 4(a) and 5(a)).

2. *Material constants by considering the strain compensation*

Flow stress depends on the temperature deformation and strain rate. Moreover, the flow stress changes with true strain (Figures 4 and 5). In addition, the effect of strain on the material constants (*i.e.*, α, β, n', and Q) is also significant during the entire strain process. Hence, it is necessary to use a method of strain compensation. In order to determine the material constants with compensated strain consideration, the values of the material constants (α, β, n', and Q) were determined from the flow curves beyond the proportionality limit, at various strains in the range from 0.05 to 0.6 (with an interval of 0.05) for all of the studied alloys. In a similar way to that described in Section I, the material constants and activation energy were extracted for the three tested alloys, using the experimental data obtained from the hot compression tests at various strains.

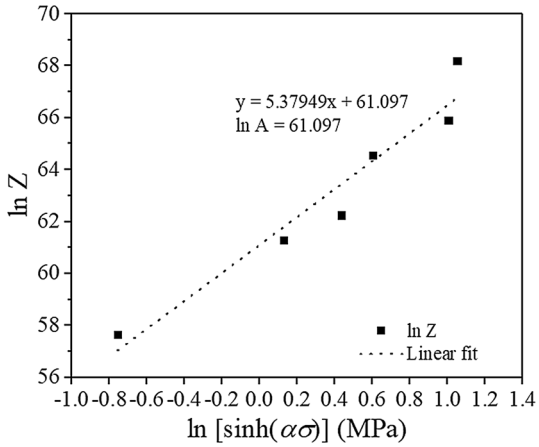

Fig. 3—Plot of ln Z – ln[sinh($\alpha\sigma$)] for the base alloy at the peak stress.

III. RESULTS

A. *Compressive True Stress–True Strain Curves*

The flow stress is an important characteristic that is defined as the instantaneous value of stress required to continue plastic deformation of an alloy, which can be related to the forgeability of the alloy. The true stress–true strain curves of experimental alloys were obtained using hot compression testing at various temperatures and strain rates and are given in Figures 4 and 5. The results show that the flow stress increases with increasing the strain rate for all tested alloys, but the flow stress decreases as the temperature increases at a given strain rate (Figures 4 and 5). In the early stage (before the peak stress reached) of isothermal

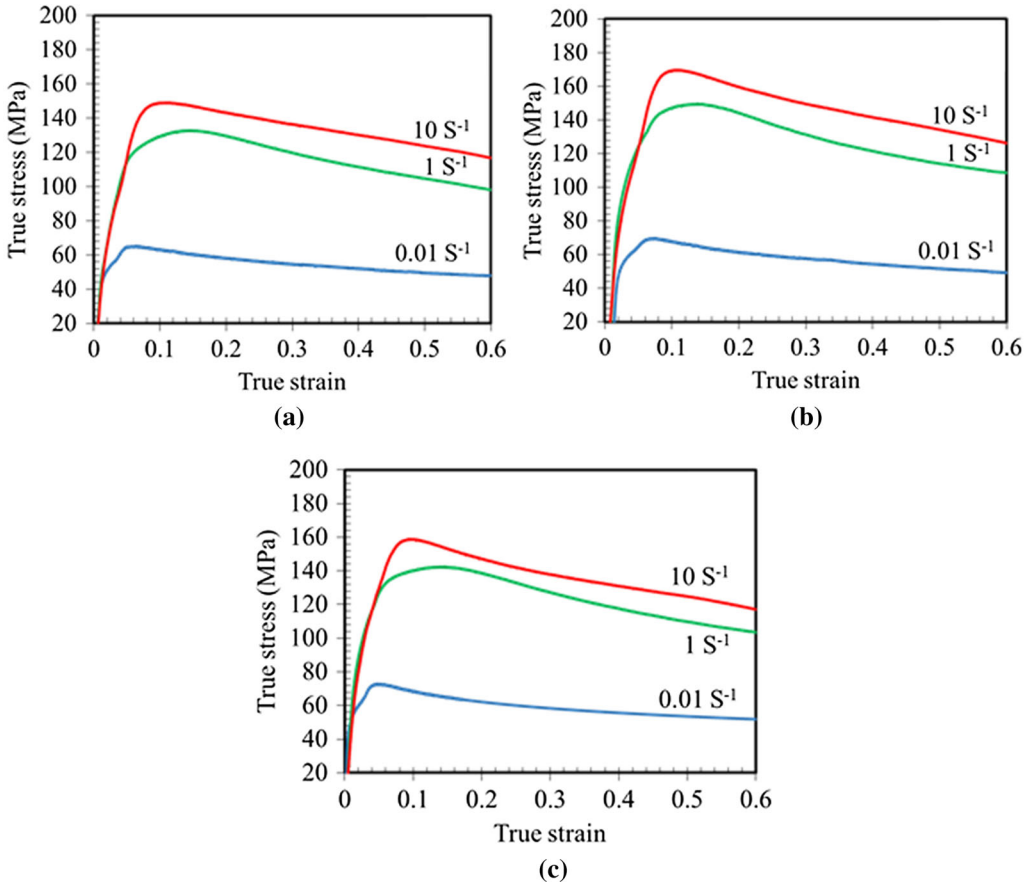

Fig. 4—Effect of strain rates on flow curves at 683 K (410 °C) of tested piston alloys: (*a*) 1Cu, (*b*) 3.5Cu, and (*c*) 3.5Cu + 0.4Er.

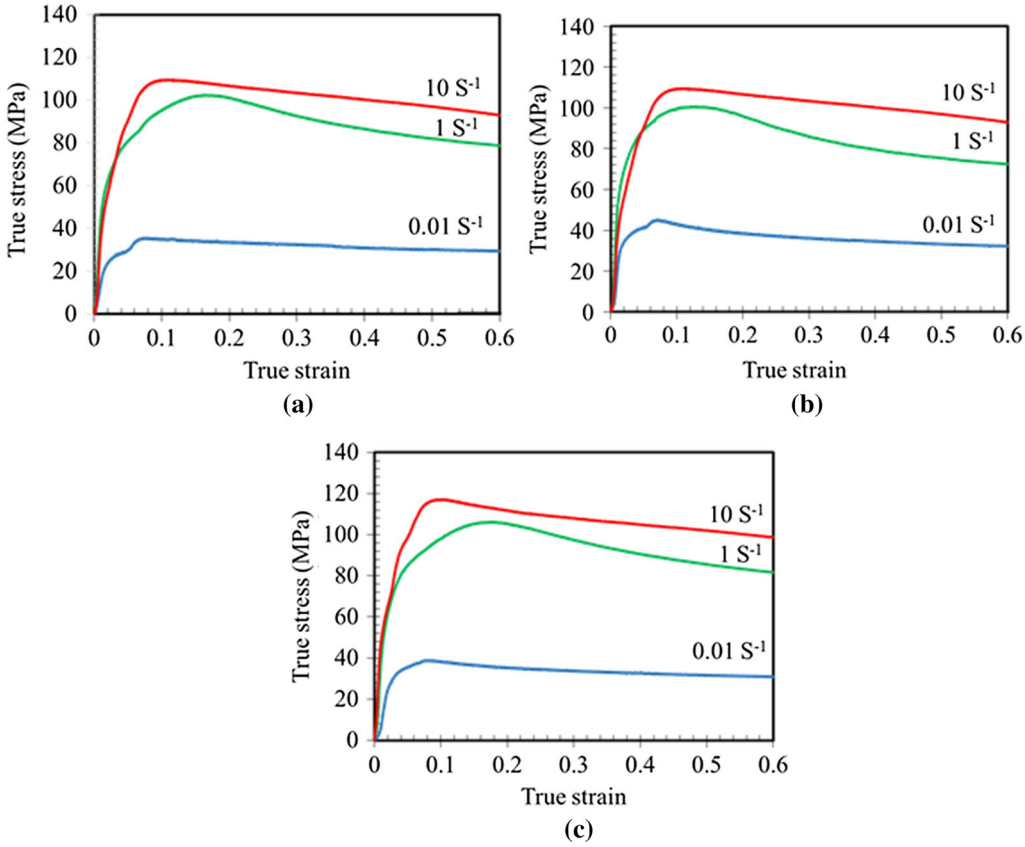

Fig. 5—Effect of strain rates on flow curves at 723 K (450 °C) of tested piston alloys: (*a*) 1Cu, (*b*) 3.5Cu, and (*c*) 3.5Cu + 0.4Er.

compressive deformation, the flow stress continues to increase with increasing strain. The flow stress of the 3.5Cu alloy is higher than those of the 3.5Cu + 0.4Er alloy and the 1Cu alloy at the high strain rate (10 s^{-1}) and low-temperature deformation [683 K (410 °C)], as observed in Figure 5. Meanwhile, upon high-temperature deformation [723 K (450 °C)], the 3.5Cu + 0.4Er alloy has a slightly higher flow stress than the other alloys. At a low strain rate (0.01 s^{-1}), the peak stress of the 3.5Cu + 0.4Er alloy is lower (before the flow stress has reached the stable state) as compared to the 3.5Cu alloy (Figures 5(b) and (c)).

B. *Deformation Parameters*

1. *Constitutive parameters*

The constitutive parameters (materials constants of A_3, α, n, and Q) in the constitutive equation (Eq. [3]) were calculated from the true stress–true strain curves, as explained in Section II–B–1. The obtained values can be substituted in Eq. [3] to get constitutive equations for all experimental alloys. Then, we can calculate the material constants at the peak flow stresses for the three alloys using the same procedure. The calculated data are shown in Table II. We examined the calculated data at the peak flow stresses because they are used as a representative value that defines the amount of energy required to initiate plastic deformation of an alloy. Then, we used the material constants based on the peak stress to obtain the constitutive equations for experimental alloys as follows (Eqs. [10] through [12]):

$$\dot{\varepsilon} = 3.42\times 1026[\sinh(0.015\sigma)]^{5.753} \exp\left(-\frac{374}{RT}\right) \text{for the 1 Cu alloy} \quad [10]$$

$$\dot{\varepsilon} = 1.36\times 1031\ [\sinh(0.013\sigma)]^{7.142} \exp\left(-\frac{436}{RT}\right) \text{for the 3.5Cu alloy} \quad [11]$$

$$\dot{\varepsilon} = 8.54\times 1023[\sinh(0.014\sigma)]^{5.854} \exp\left(-\frac{338}{RT}\right) \text{for the 3.5Cu + 0.4Er alloy} \quad [12]$$

These constitutive equations of each alloy (Eqs. [10] through [12]) can be used to predict the flow behavior of AA4032 with low and high Cu content and with Er addition at elevated temperatures.

The material constants with compensated strain are shown in Figures 6 and 7. It is quite clear that the strain effect on the material constants is significant and the values of Q are affected by strain for the three tested alloys. The influence of strain can be expressed as a polynomial function of strain,[28] as given in Eqs. [13] through [16] for the six-order polynomial fit. A

Table II. Material Constants in Constitutive Equation of Experimental Alloys at the Peak Stress

Alloys	A_3	α (MPa^{-1})	n'	Q (kJ/mol)
1Cu (The Base Alloy)	3.42×10^{26}	0.015	5.753	374
3.5Cu	1.36×10^{31}	0.013	7.142	436
3.5Cu-0.4Er	8.54×10^{23}	0.014	5.854	338

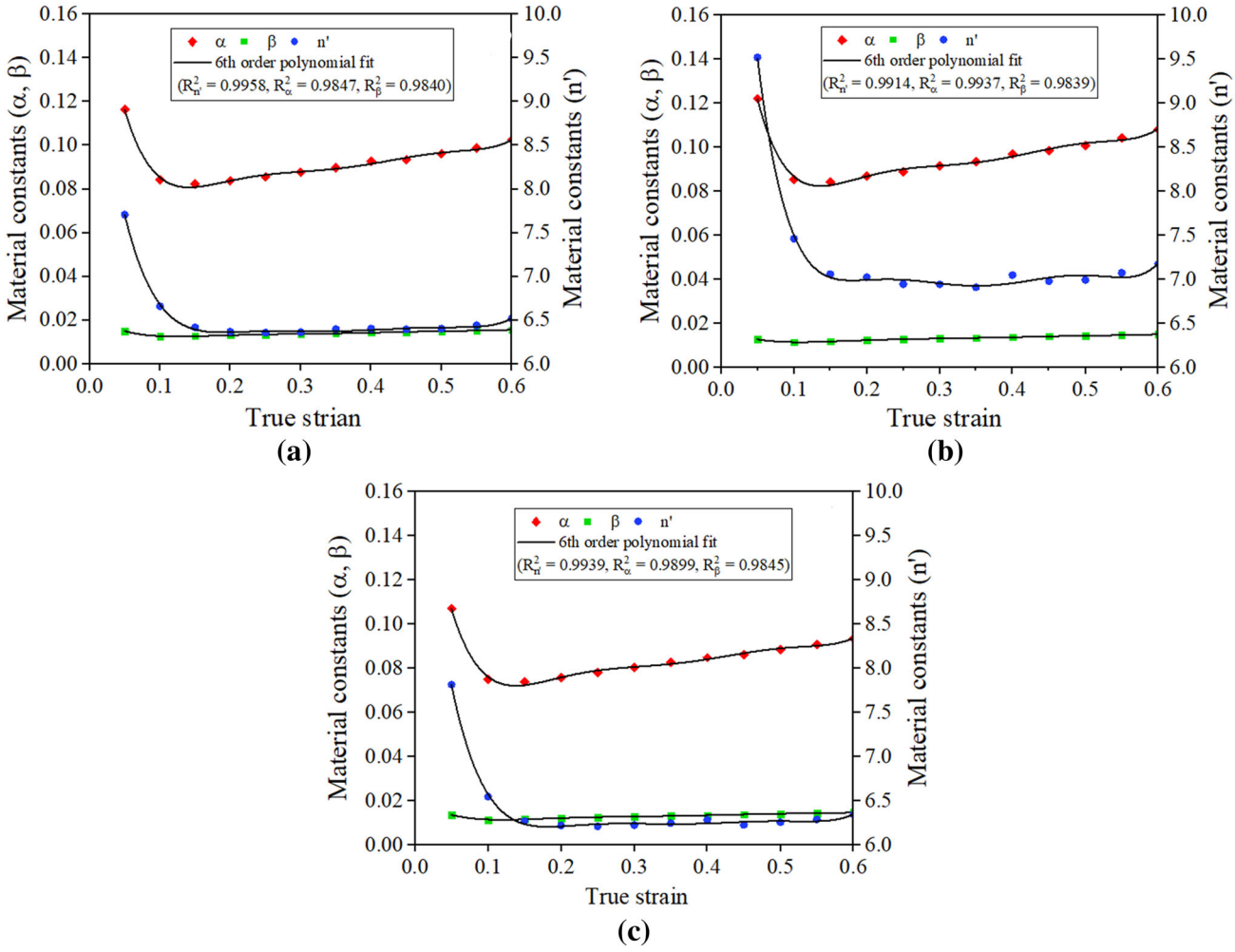

Fig. 6—Values of n', α, and β at different true strain levels and the fitted curves by the six-order polynomial equation of the tested piston alloys: (*a*) 1Cu, (*b*) 3.5Cu, and (*c*) 3.5Cu + 0.4Er.

polynomial fit of a higher order (*i.e.*, higher than six order) could be used, but it will overfit the data, resulting in loss of the ability to have a true physical meaning of the data.[29] On the other hand, a lower-order polynomial fit may also be used to accurately represent the experimental result if the data permits.[30] Our result shows that the best fit is attained through a six-order polynomial fit. The coefficients of the polynomial fit are given in Electronic supplementary Table S1. Figures 6 and 7 demonstrate that the fitted curves agree well with the results calculated from the experimental data.

$$n' = a_0 + a_1\varepsilon + a_2\varepsilon^2 + a_3\varepsilon^3 + a_4\varepsilon^4 + a_5\varepsilon^5 + a_6\varepsilon^6 \quad [13]$$

$$\alpha = b_0 + b_1\varepsilon + b_2\varepsilon^2 + b_3\varepsilon^3 + b_4\varepsilon^4 + b_5\varepsilon^5 + b_6\varepsilon^6 \quad [14]$$

$$\beta = c_0 + c_1\varepsilon + c_2\varepsilon^2 + c_3\varepsilon^3 + c_4\varepsilon^4 + c_5\varepsilon^5 + c_6\varepsilon^6 \quad [15]$$

$$Q = d_0 + d_1\varepsilon + d_2\varepsilon^2 + d_3\varepsilon^3 + d_4\varepsilon^4 + d_5\varepsilon^5 + d_6\varepsilon^6 \quad [16]$$

2. *Activation energy (Q)*

The hot deformation activation energy is an important physical parameter serving as an indicator of the deformation difficulty degree in plasticity deformation.

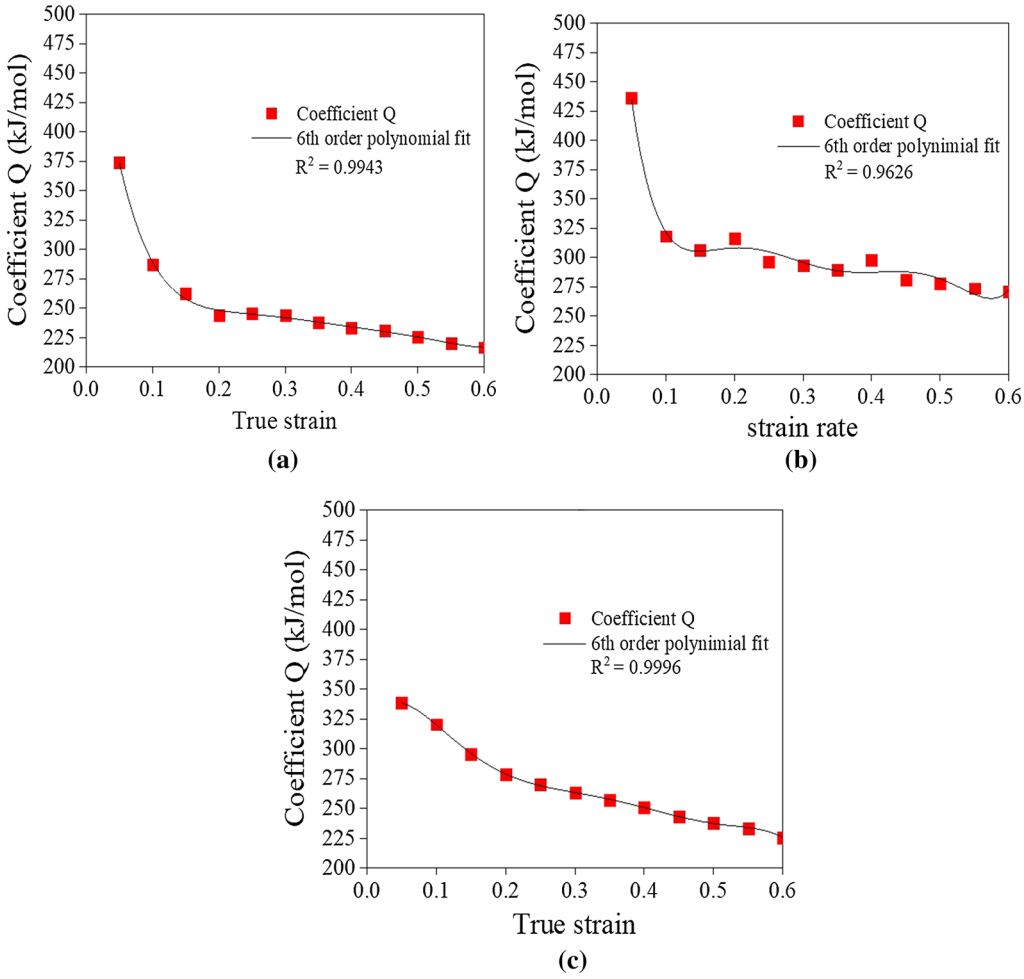

Fig. 7—Activation energy at different true strain levels and the fitted curves by the six-order polynomial equation of the tested piston alloys: (*a*) 1Cu, (*b*) 3.5Cu, and (c) 3.5Cu + 0.4Er.

Thus, in order to estimate the activation energy for hot deformation of the tested alloy, the Q values were obtained using Eq. [7]. The values of activation energy at different strains (ranging from 0.1 to 0.6 with an interval of 0.1), strain rates (0.01 to 10 s^{-1}), and temperatures [683 K to 723 K (410 °C to 450 °C)] were calculated and are shown in Figure 7 and Table II. The activation energy of the 3.5Cu alloy at the peak strain is about 436 kJ/mol, which is higher than that of the base alloy (374 kJ/mol). However, the 3.5Cu + 0.4Er alloy has an activation energy of 338 kJ /mol, *i.e.*, lower than those of other tested alloys. The activation energies at other strains follow the same trend (Figure 7).

3. *The strain-rate sensitivity (m) under various parameters*

Strain-rate sensitivity is one of the important constitutive parameters that is used to predict the sensitivity of the alloys to the changes of the strain rate during hot deformation. We can take the ln of both sides of Eq. [1], and the slope of $\ln \sigma$–$\ln \dot{\varepsilon}$ curves will give us a strain-rate sensitivity (m) for each alloy. These values are given in Figure 8. The results show that the strain-rate sensitivity is reduced sharply with the increase in the Cu content, while the further addition of Er increases the values slightly above the base alloy for all true strains during compressive tests (at the strain-rate range of 0.1 to 10 s^{-1} and temperatures (683 K to 723 K (410 °C to 450 °C)).

4. *Z parameter (Z)*

The ln Z values of the deformed samples under different deformation conditions were obtained from Eqs. [8] and [9] and are given in Table III. The results show that the Z parameter increases with decreasing temperature and increasing strain rate. Also, the increased amount of Cu considerably increases the Z parameter, while the addition of Er decreases the values to levels lower than those of the base alloy.

C. *Microstructural and Compositional Analysis*

Figure 9 shows optical micrographs of the as-cast AA4032-type alloys with different levels of Cu and Er additions. The results reveal that when Cu is added up to 3.5 wt pct into the base Al-Si piston alloy (AA4032) (Figure 9(a)), the microstructure consists of primary Si particles and coarse eutectic phases including Si and the

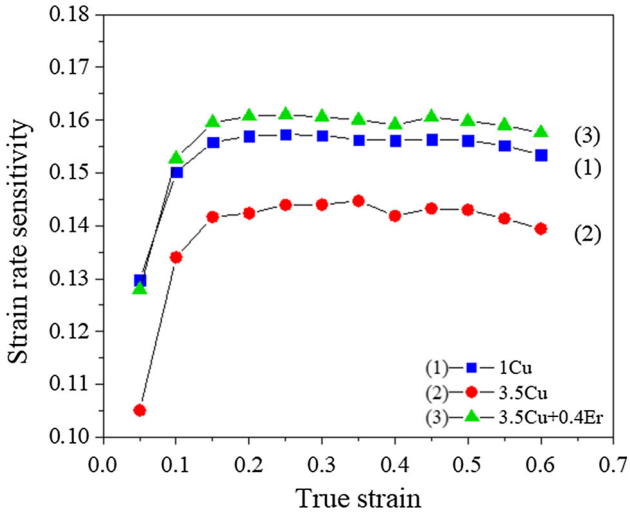

Fig. 8—Strain-rate sensitivity of three experimental alloys under hot deformation conditions.

Table III. Values of ln *Z* at the Peak Stress under Different Deformation Conditions

Alloys	Temperature K (°C)	Strain Rate (s^{-1}) 0.01	1	10
1Cu	683 (410)	61.30	65.90	68.20
	723 (450)	57.65	62.25	64.56
3.5Cu	683 (410)	72.33	76.93	79.23
	723 (450)	68.07	72.68	74.98
3.5Cu + 0.4Er	683 (410)	54.96	59.56	61.86
	723 (450)	51.66	56.27	58.57

Al matrix (Figure 9(b)). The addition of 0.4 wt pct Er to the AA4032 with 3.5 wt pct Cu content reduces the amount of primary Si particles and refines the eutectic phases (Figure 9(c)) as compared to the base alloy (Figure 9(a)) and the 3.5Cu alloy without Er addition (Figure 9(b)). The in-depth analysis of these changes in the phase composition has been reported elsewhere.[10]

Due to the rapid cooling rate in the DC casting, the alloying elements may remain in a supersaturated solid solution. Therefore, the difference in constitutive behavior may be attributed to the supersaturation of alloying elements in the aluminum solid solution and the phase precipitation during hot deformation. The phase diagram can be used to estimate the chemical composition of the supersaturated solid solution after solidification.[31] The decomposition of this supersaturated solid solution at the temperatures of hot deformation leads to the precipitation of phases that affect the hardening and softening mechanisms. Thermo-Calc software (TCAL4 database) was used to calculate the composition of the Al solid solution at a temperature of the end of solidification for an AA4032 alloy. The calculated results gave the following composition of the solid solution in the 3.5Cu alloy at 803 K (530 °C): 1.5 wt pct Cu, 1 wt pct Si, and 0.55 wt pct Mg. Then, we used the composition of this solid solution to assess the

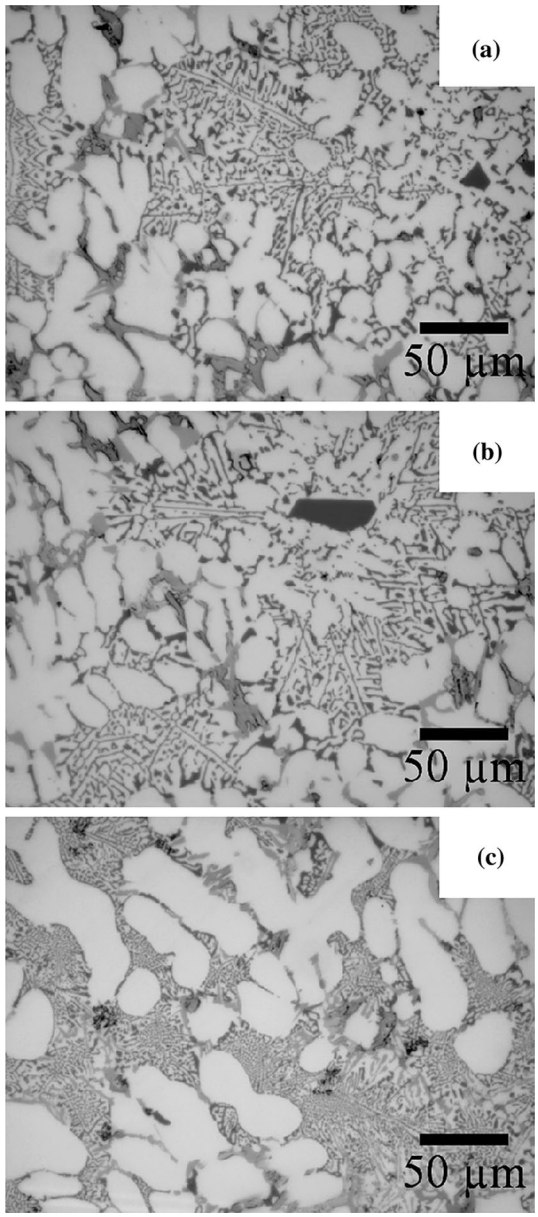

Fig. 9—Optical micrographs showing the initial microstructure of as-cast alloys: (*a*) 1Cu (base) alloy, (*b*) 3.5Cu, and (*c*) 3.5Cu + 0.4Er.

formation of phases upon annealing at testing temperatures of 683 K to 723 K (410 °C to 450 °C), which showed the formation of Si, γ-Al_7Cu_4Ni, and Q-$Al_5Cu_2Mg_8Si_6$ phases, as can be seen in Table IV. The volume fraction of the phases that remain in the microstructure at high temperature can be related to the high activation energy of the alloy. This agrees with another study on an Al-Si-Ni-Cu-Mg alloy that reported that the high volume of dispersed particles resulted in the increased activation energy.[32] We do not expect significant changes in these compositions for the alloy with Er, apart from the possible formation of Er-containing dispersoids that cannot be estimated from Thermo-Calc. The results on the composition of the solid solution can also be used to analyze the

recrystallization behavior by comparing our alloys with alloys of the similar solid solution composition, *e.g.*, AK6 (1360) and AA2038.

To gain deeper understanding of the deformation mechanism of these alloys, the 3.5Cu alloy and 3.5Cu + 0.4Er alloy specimens deformed at 450 °C at strain rates of 0.01 and 10 s^{-1} were analyzed using the EBSD technique to observe the microstructure. Figure 10 shows the SEM images of Al grains and eutectic phases after deformation of the 3.5Cu alloy at a strain rate of 0.01 s^{-1} (Figure 10(a)) and at a strain rate of 10 s^{-1} (Figure 10(d)). The EBSD-generated inverse pole figure (IPF) maps superimposed with HAGBs and LAGBs are shown for the enlarged areas from SEM images (areas I through IV in Figures 10(a) and (d)), representing subgrain structure after hot deformation (Figures 10(b) and (c) for 0.01 s^{-1} and (e) and (f) for 10 s^{-1}). The different colors in IPF images represent different orientations of grains and subgrains inside the original grains. All the IPF images of the 3.5Cu alloy (Figures 10(b), (c) and (e), (f)) show fine elongated grains along with coarse intermetallics, eutectic Si phases, and primary Si particles. The dark areas on all of the IPF maps represent either intermetallics or cracks of the deformed microstructures. It can be seen that the 3.5Cu alloy that was deformed at a strain rate of 0.01 s^{-1} (Figures 10(b) and (c)) has cracks or voids encircling the primary Si particles, while in the same alloy that was deformed at a strain rate of 10 s^{-1} (Figures 10(e) and (f)), the primary Si particles were fully cracked and the intermetallics and coarse eutectic phases had started to tear (dark area in IPF images) along the Al grain.

The SEM micrographs and the IPF maps for the 3.5Cu + 0.4Er alloy are exhibited in Figure 11. The IPF images show that the grains are deformed and contain subgrains within the original boundaries (Figures 11(b) and (c) for 0.01 s^{-1} and (e) and (f) for 10 s^{-1}) of the enlarged areas (areas I through IV in Figures 11(a) and (d)). Figures 11(e) and (f) show that the fraction of recrystallized grains increases when the alloy is deformed at a high strain rate of 10 s^{-1}. However, in general, the 3.5Cu alloy has more recrystallized grains as compared to the one with Er addition, especially at a lower strain rate.

To further analyze the recrystallization behavior, the deformed grains were quantified with the average boundary misorientation angle. The number fractions of LAGBs (misorientation angle less than 5 deg) and HAGBs (misorientation angle greater than 15 deg) were used to analyze the microstructure and ultimately can be used to quantify the extent of recrystallization in the alloys after hot deformation. The comparison of the grain boundary misorientation angles of two different alloys is shown in Figure 12. In general, the misorientation angle has similar trends for both alloys with and without Er addition, having more HAGBs than LAGBs. However, at a low strain rate of 0.01 s^{-1}, the alloy with Er addition has a lower fraction of HAGBs as compared to the 3.5Cu alloy with correspondingly more LAGBs. Meanwhile, the fraction of HAGBs of the 3.5Cu + Er alloy at a high strain rate of 10 s^{-1} is similar to the alloy without Er.

IV. DISCUSSION

The obtained constitutive parameters have value in their own right as they can be used in improving the computer simulation of the forging process. In addition, the analysis of some of these parameters can shed light on the mechanisms of deformation and recrystallization of these alloys and the role of alloying elements, such as Cu and Er, on these mechanisms.

The flow curve behavior can be affected by work hardening, which results from the presence of solute atoms, secondary phases, and their interaction with dislocation movement. The softening that occurs in the steady stage of the flow curve is usually caused by recovery and recrystallization. The results in Figures 4 and 5 show that the flow stress increases rapidly with the strain in the initial stage of hot deformation, indicating the work hardening was caused most likely by the rapid increase of dislocation density.[1] In all cases tested, the flow stress increased with the increase of strain rate and the decrease of deformation temperature, which agrees well with previous reports.[33,34] Our experiments show that the flow stress and the peak stress increase with the Cu content in the alloy, while they decrease with Er addition. The increase of the flow stress of the 3.5Cu alloy can be related to the presence of hard particles, *i.e.*, primary Si, and the solid solution strengthening by Cu, Mg, and Si (Table IV) due to the solute drag effect on dislocation movement, which hinders DRV.[35,36] Moreover, our results agree with the previous work that reported that the increased amount of primary Si particles resulted in a large amount of geometric dislocation around hard particles in the soft Al matrix, which ultimately impedes deformation.[37] The observed decrease of the flow stress of the 3.5Cu + 0.4Er alloy as compared to the 3.5Cu alloy at both low and high strain rates (Figure 4(c)) is, therefore, due to the decrease in the amount of primary Si particles and the refinement of eutectic phases (Figure 9), which results in a homogenous initial microstructure (Reference 10 provides more details). The positive impact of a more uniform eutectic silicon morphology on the flow behavior was also reported elsewhere.[38] At elevated temperatures, dislocation climb commonly occurs, which leads to the decrease in flow stress.[39] However, we found that, at 723 K (450 °C) and 10 s^{-1}, the 3.5Cu + 0.4Er alloy shows a slightly higher flow stress than the alloy without Er. This can be explained by the presence of fine Er precipitates that may form during hot deformation and stabilize the substructure, impeding dynamic softening processes while simultaneously marginally increasing the strain hardening rate.[2,16] The effects of Cu and Er on the microstructure evolution and phase composition of as-cast AA4032 alloys are described in detail elsewhere.[10]

The activation energy Q represents the free energy barrier for dislocations moving on slip planes and indicates the deformation resistance of materials. As the activation energy of self-diffusion in Al is approximately 142 to 165 kJ/mol[40,41] and the estimated Q in our alloys is 1.5 to 2 times larger (Figure 7), additional factors to diffusion-controlled deformation should be in play. The

Table IV. Calculated Chemical Compositions of Supersaturated Solid Solution (for 803 K (530 °C)) and the Phases Formed at 683 K to 723 K (410 °C to 450 °C)

	Alloy Composition (Wt Pct)			Supersaturated Solid Solution Composition (Wt Pct)			Possible Phases Formed at Elevated Temperatures 683 K to 723 K (410 °C to 450 °C)	Volume Fraction Phases Formed at Elevated Temperatures 683 K to 723 K (410 °C to 450 °C)
Alloy	Si	Cu	Mg	Si	Cu	Mg	Si	0.1334 to 0.1343
3.5Cu	12.9	3.5	1	1	1.5	0.5	γ-Al_7Cu_4Ni Q-$Al_5Cu_2Mg_8Si_6$	0.0324 to 0.0386 0.0227 to 0.0016

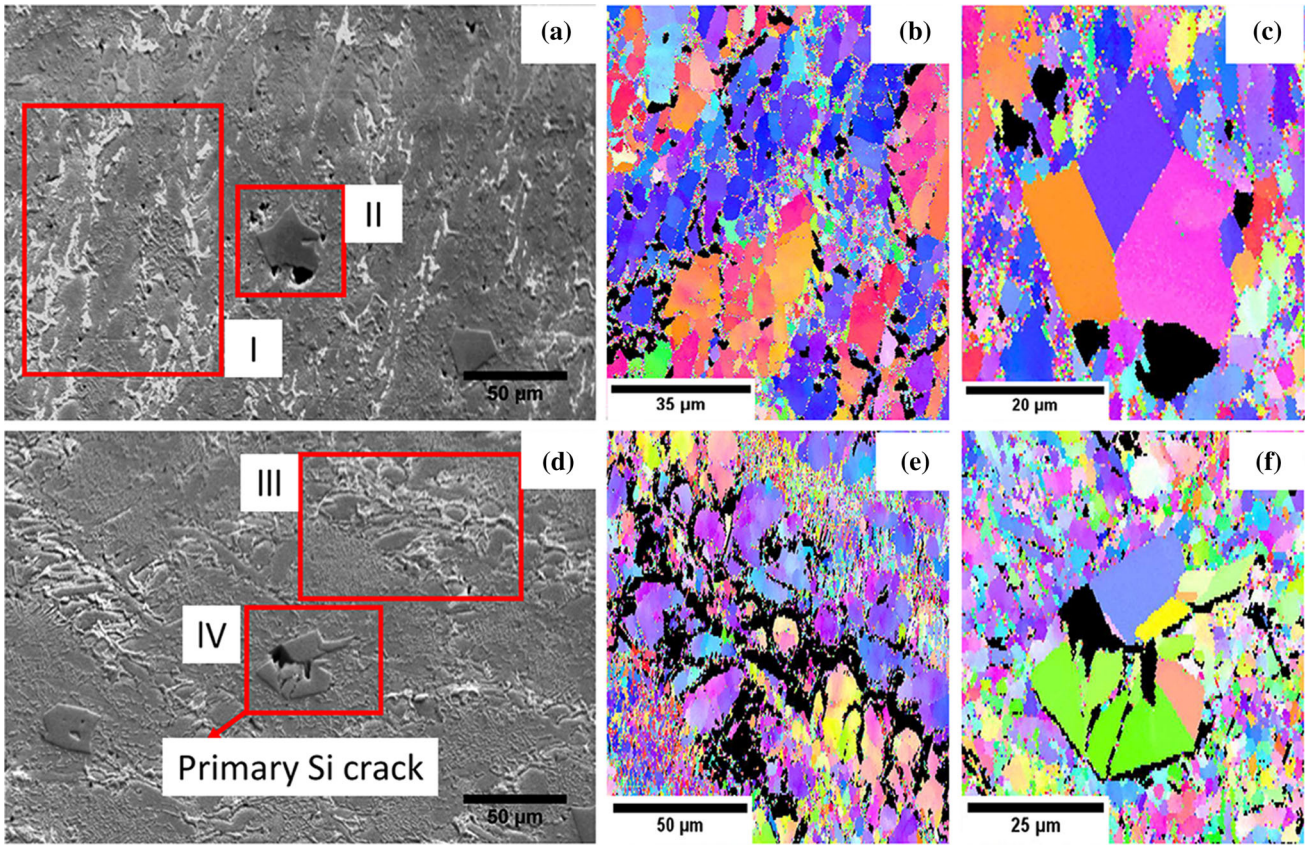

Fig. 10—SEM and EBSD images of the specimens deformed at the high temperature (450 °C) of the 3.5Cu alloy at a strain rate of 0.01 s^{-1}: (*a*) SEM image, (*b*) subgrain of area I, and (*c*) deformed primary Si crystal in area II in (a); and at strain rates of 10 s^{-1}: (*d*) SEM image, (*e*) subgrain of area III, and (*f*) primary Si crystal crack in area IV in (b).

high values of activation energy can be related to the presence of precipitates, the morphology of eutectic phases, and other particles in the microstructure, which cause the strengthening of an alloy.[33,38]

The AA4032 alloys with Cu and Cu + Er additions exhibit relatively high values of the activation energy (Q) in comparison with other aluminum alloys, which have similar compositions. In our study, the base alloy (1Cu alloy) has Q between 216 and 374 kJ/mol (at strains 0.05 to 0.6) (Figure 7(a)), which is similar to the reported Q values of an AA4032 alloy, between 169 and 325 kJ/mol (at strains 0.1 to 0.5) depending on the strain rate.[6] Our results found that Q of the 3.5Cu alloy increases to 270 to 436 kJ/mol (Figure 7(b)), which is higher than that of the base alloy. This is consistent with the previous work that reported the increase of the activation energy from 283 to 315 kJ/mol in an Al-7Si-1Cu-0.5Mg-0.1Ti (wt pct) base cast alloy with the additions of V and Zr.[42] This was explained from the solute atoms diffusing to dislocations and slowing the dislocation motion. This also agrees with previous reports that show that Cu additions in an 6A82 aluminum alloy (Al-Mg-Si-Cu) and Al-Fe-Si alloy increase the Q values.[35,43] In our case, the increased activation energy of the 3.5Cu alloy may be caused by solute Si, Mg, and Cu atoms that decrease stacking fault energy (SFE), resulting in the

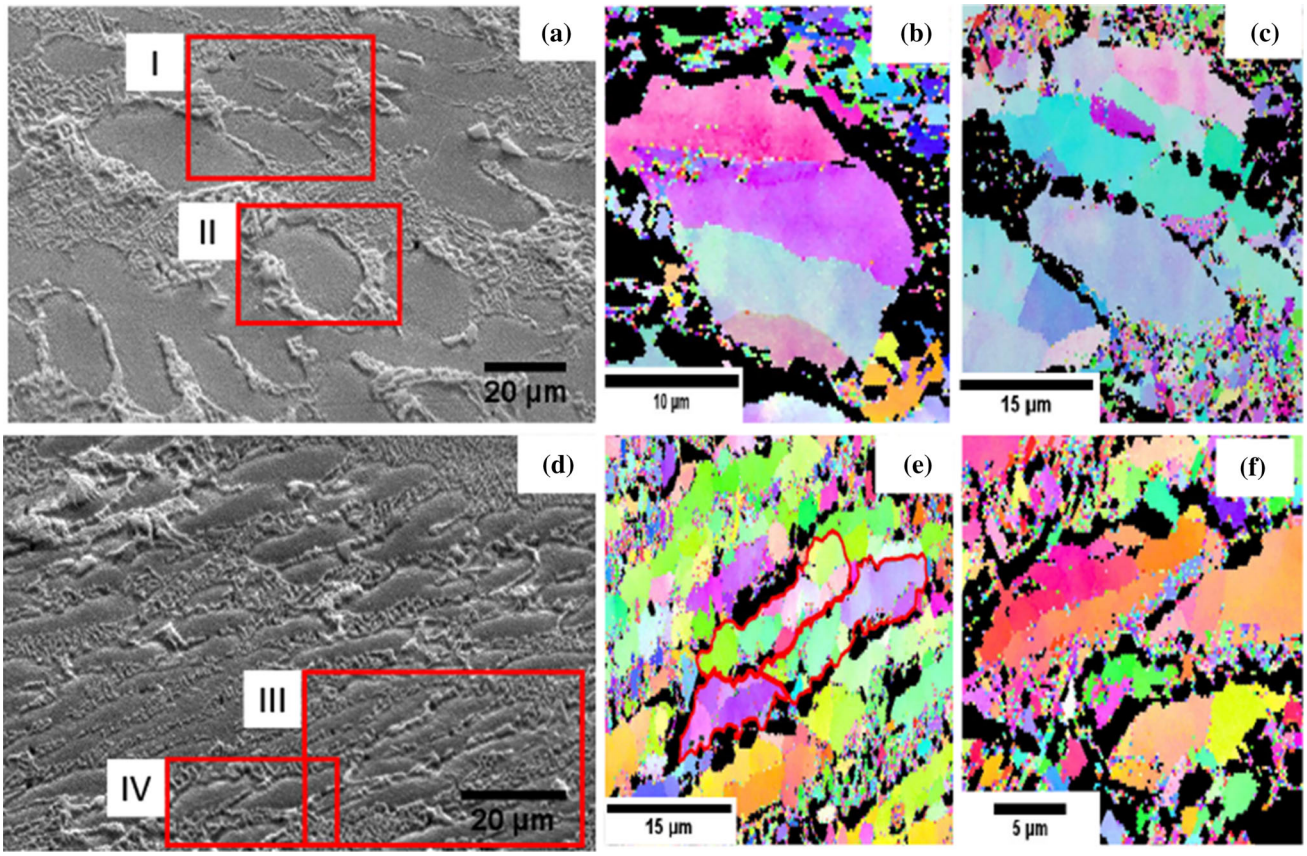

Fig. 11—SEM and EBSD images of the specimens deformed at high-temperature deformation (450 °C) of the 3.5Cu + 0.4Er alloy at strain rates of 0.01 s^{-1}: (*a*) SEM image, (*b*) IPF of subgrain area I, and (*c*) IPF of subgrain area II in (a); and at strain rates of 10 s^{-1}: (*d*) SEM image, (*e*) IPF of subgrain area III, and (*f*) IPF of subgrain area IV in (b).

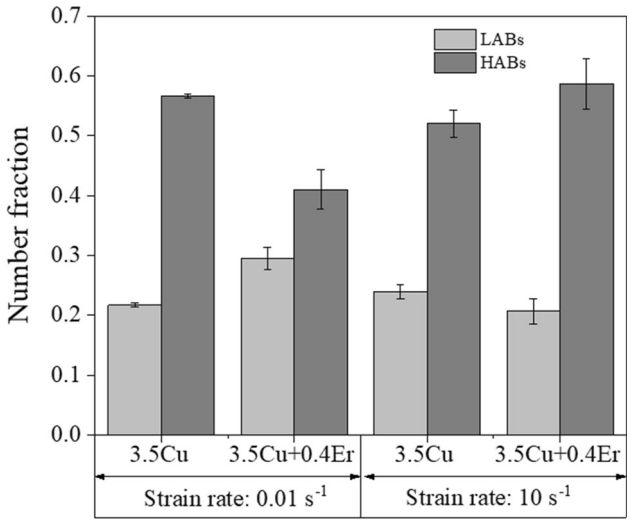

Fig. 12—Comparison of the number fraction of grain boundary misorientation angles of the 3.5Cu and the 3.5Cu + 0.4Er alloys at a low strain rate of 0.01 s^{-1} and high strain rate of 10 s^{-1}: LAGBs (2 to 15 deg) and HAGBs (> 15 deg).

hindered dislocation movement and recovery.[44] However, the addition of Er in the 3.5Cu + 0.4Er alloy decreases Q to 225 to 338 kJ/mol (at strains 0.1 to 0.5) (Figure 7(c)), which is closer to the base alloy (216 to 374 kJ/mol). This cannot be explained from the effects of Er on the SFE as this effect is rather small.[45]

On the other hand, the addition of Er results in significant structure refinement (Figure 9), which leads to enhanced ductility.[7] Therefore, the addition of Er enables deformation under a lower applied stress and requires less activation energy for deformation. In general, the differences of activation energy may result from the concurrence of dynamic precipitation, dislocation pinning effect, temperature dependence of the solubility of alloying elements, and overall structural fineness. Hence, the activation energy not only depends on the temperature and strain rate but also relates to the nature and amount of alloying elements. The result obtained here suggests that the 3.5Cu + 0.4Er alloy has better formability compared to the 3.5Cu alloy, while still having flow stress higher than the base alloy, especially when the alloys are deformed at low temperature and high stain rate (Figures 4(a) and (c)).

The physical significance of the strain-rate sensitivity (m) is to signal the alloy sensitivity to the strain rate and characterize plasticity during deformation. It was reported that when m values increase with temperature, this suggests that the alloys are more sensitive to the strain rate.[6] Moreover, the additions of solute atoms to an aluminum alloy are influential to this value.[46] It was

reported that the strain-rate sensitivity parameter decreased with an increase in the amount of solute atoms such as Mg and Si. This is due to the dislocation arrest at obstacles such as clusters of mobile solute atoms and solute precipitation. The pipe diffusion of these solute atoms encourages the generation of dislocation atmospheres.[46,47] According to the calculated results using Thermo-Calc, the 3.5Cu alloy contains 1.5 wt pct Cu, 0.55 wt pct Mg, and 1 wt pct Si at 803 K (530 °C) in solid solution and may form a supersaturated solid solution upon solidification (cooling rates are high during DC casting); a similar composition of the solid solution should be in the alloy with Er as well. When the alloys are deformed at 683 K to 723 K (410 °C to 450 °C), the solute atoms of Si, Cu, and Mg combine to precipitate Q-$Al_5Cu_2Mg_8Si_6$ and Si phases from the supersaturated solid solution, and then these precipitates act as barriers to the mobility of dislocations. This effect is similar with other work that reported the pinning effect of Mn- and Cr-containing α-dispersoids on dislocation motion.[7] Moreover, the addition of Er to the 3.5Cu alloy may retard the precipitation of new phases during deformation because the diffusivity of Er is lower than the those of elements in α-Al at 673 K (400 °C) ($D_{Er} = 4 \times 10^{-19}$ m^2/s $< D_{Si} = 5.67 \times 10^{-15} < D_{Cu} = 2.5 \times 10^{-15}$ m^2/s $< D_{Mg} = 1.16 \times 10^{-14}$).[48,49] It was suggested that the increasing strain-rate sensitivity may be a result of less free solute atoms. In our previous research,[10] we showed that the Er interacts with Cu during solidification to form intermetallics. This may reduce the free solute Cu available during hot deformation. Thus, the 3.5Cu alloy has more solute atoms available to interact with dislocations and form atmospheres, which results in a higher stress to move dislocations. This may be responsible for reducing the strain-rate sensitivity (Figure 8) and increasing the flow stress (Figures 4 and 5) and activation energy (Figure 7) in the 3.5Cu alloy in comparison with the base alloy and the 3.5Cu + 0.4Er alloy.

It is well known that the flow behavior of the alloys is attributed to the interaction of several mechanisms, including work hardening and softening with DRV or DRX, which requires further microstructural observation.[3,13] The Z parameter is the main parameter that is used to describe the relationship between the temperatures, strain rate, and microstructural evolution after hot deformation. In all cases of deformation tests, the Z values of our alloys (Table III) show the decrease with the increasing deformation temperature or the decreasing strain rate. This corresponds to the Z values decreasing with the relative flow stress decreasing, which is represented in terms of $\ln[\sinh(\alpha\sigma)]$ (Figure 3) with decreasing the Z values. In other words, the low Z values demonstrate that there is sufficient time for DRV and the high Z values indicate that DRX may occur during the deformation stage, so that there is a considerable softening in agreement with previous reports.[50] Our results show that the 3.5Cu + 0.4Er alloy has slightly lower Z values than the 3.5Cu alloy; this indicates that the 3.5Cu + 0.4Er alloy responds better to the softening mechanism than the 3.5Cu alloy. This is also consistent with the results on the decrease of the flow stress and activation energy of deformation.

Additionally, EBSD is generally used to analyze the deformation mechanism and recrystallization. Our results show that the hot-deformed 3.5Cu alloy has mostly recrystallized structure and fractures primary Si when deformed at a high strain rate (Figures 10(c) and (f)). This agrees well with the previous work, which reported that the increasing strain rate caused primary Si cracks in the microstructure.[17] The results also show that the grain misorientation changes from LAGBs to HAGBs, indicating that the recrystallization occurs in the deformed samples. Our results found that at a low strain rate, the number fraction of HAGBs of the 3.5Cu alloy is higher than the 3.5Cu + 0.4Er alloy (Figure 12 at a strain rate of 0.01 s^{-1}), which indicates that the recrystallization may be the main restoration mechanism for the 3.5Cu alloy, while the 3.5Cu + 0.4Er alloy experiences recovery and polygonization. This may be due to the action of fine dispersed Al_3Er precipitates formed from the supersaturated solid solution during deformation, which pin the dislocations and the subgrain boundaries; therefore, the recrystallization behavior is restrained. This is consistent with previous work, which reported that fine particles of Al_3Er can pin the dislocation movement and the grain boundary slide, resulting in restrained recrystallization.[16] Meanwhile, the 3.5Cu alloy has a similar fraction of HAGBs as the 3.5Cu + 0.4Er alloy at a higher strain rate. This may be due to a larger accumulated stress that triggers recrystallization due to lesser time being available for polygonization and recovery. Fine Q-phase precipitates can pin down grain boundaries and impede the grain growth as well.[43] There is also less time for solute diffusion to dislocations. Hence, the softening mechanism of the 3.5Cu + Er alloy exhibits partial polygonization at lower strain rates and recrystallization at higher strain rates. In general, the number fraction of HAGBs is higher than LAGBs for both alloys, which means that recrystallization is the main softening mechanism during hot deformation in these aluminum alloys.

These observations are consistent with the processing map of an AK6 alloy, which has a similar composition as the solid solution composition in our alloy. It was reported that the increase in the strain rate [in the temperature range 673 K to 773 K (400 °C to 500 °C)] resulted in the softening mechanism changing from mixed polygonization and recrystallization to full recrystallization.[51] Our results demonstrate that the deformation and recrystallization mechanisms are sensitively dependent on deformation temperature, strain rate, alloying elements, precipitated phases, and morphology of phases in the initial microstructure.

V. CONCLUSIONS

1. The compressive flow stress in AA4032-type alloys increases with increasing strain rate and decreasing deformation temperature, which is described by a constitutive equation as a hyperbolic sine function with the activation energy.

2. The material constants in the constitutive equation are derived and can be used to predict the flow behavior of AA4032-type alloys, also with Cu and Er additions, at elevated temperatures.
3. The peak stress increases during hot deformation with increasing Cu content.
4. The flow behavior of the base AA4032 alloy and the alloy with high Cu addition reflects nonuniform microstructure (primary Si particles).
5. The hot deformation activation energy (at a peak stress) for the AA4032 alloy with high Cu content increases to 437 kJ/mol as compared to 374 kJ/mol for the base alloy. An addition of 0.4 wt pct Er to the high-Cu alloy decreases the activation energy to the level lower than that of the base alloy, *i.e.*, to 338 kJ/mol.
6. The EBSD results show that at a high strain rate of 10 s^{-1}, the 3.5Cu + 0.4Er alloy has a similar fraction of recrystallized grains in comparison to the base alloy and the 3.5Cu alloy. Meanwhile, the Er containing alloy shows polygonization and partial recrystallization at a lower strain rate. The polygonization and recrystallization are the main softening mechanisms in these alloys upon hot deformation.

ACKNOWLEDGMENTS

This work was financially supported by The Research and Researchers for Industry (RRi) under the Thailand Research Fund (TRF), which offers a scholarship for a Ph.D. student (received by author SC) (PHD57I0060) with Thai Metal Aluminium Co., Ltd. together with additional support from King Mongkut's University of Technology Thonburi through the "KMUTT 55th Anniversary Commemorative Fund." SC also gratefully acknowledges BCAST (UK) for hosting the research visit.

ELECTRONIC SUPPLEMENTARY MATERIAL

The online version of this article (https://doi.org/10.1007/s11661-019-05482-9) contains supplementary material, which is available to authorized users.

OPEN ACCESS

REFERENCES

1. M. Zhou and M.P. Clode: *Mech. Mater.*, 1998, vol. 27, pp. 63–76.
2. H.J. McQueen, S. Spigarelli, M.E. Kassner, and E. Evangelista: *Hot Deformation and Processing of Aluminum Alloys*, CRC Press, Boca Raton, FL, 2016.
3. H.J. McQueen and W. Blum: *ICAA-6: 6th International Conference on Aluminium Alloys,* 1998, pp. 99–112.
4. L. Zhen, H. Hu, X.-Y. Wang, B. Zhang, and W. Shao: *J. Mater. Process. Technol.*, 2009, vol. 209, pp. 754–61.
5. L. Ou, Z. Zheng, Y. Nie, and H. Jian: *J. Alloys Compd.*, 2015, vol. 648, pp. 681–89.
6. G. Fang and P. Zeng: *J. Mater. Eng. Perform.*, 2006, vol. 15, pp. 535–39.
7. Y. Xu, H. Nagaumi, Y. Han, G. Zhang, and T. Zhai: *Metall. Mater. Trans. A*, 2017, vol. 48A, pp. 1355–65.
8. M. Murayama, K. Hono, W. Miao, and D.E. Laughlin: *Metall. Mater. Trans. A*, 2001, vol. 32A, pp. 239–46.
9. K. Matsuda, S. Ikeno, Y. Uetani, and T. Sato: *Metall. Mater. Trans. A*, 2001, vol. 32A, pp. 1293–99.
10. S. Chankitmunkong, D.G. Eskin, U. Patakham, and C. Limmaneevichitr: *J. Alloys Compd.*, 2019, vol. 782, pp. 865–74.
11. M. Colombo, E. Gariboldi, and A. Morri: *J. Alloys Compd.*, 2017, vol. 708, pp. 1234–44.
12. Z.M. Shi, Q. Wang, G. Zhao, and R.Y. Zhang: *Mater. Sci. Eng., A,* 2015, vol. 626, pp. 102–107.
13. Y.C. Lin and X.-M. Chen: *Mater. Des.*, 2011, vol. 32, pp. 1733–59.
14. H. Mirzadeh: *Mech. Mater.*, 2015, vol. 85, pp. 66–79.
15. L. Chen, G. Zhao, and J. Yu: *Mater. Des.*, 2015, vol. 74, pp. 25–35.
16. M. Gang: *Mater. Sci. Eng., A*, 2009, vol. 516, pp. 131–37.
17. X. Hu, B. Yang, J. Xu, and H. Wang: *Mater. Sci. Forum*, 2013, vol. 749, pp. 88–95.
18. L. Saravanan and T. Senthilvelan: *J. Mater. Res. Technol.*, 2016, vol. 5, pp. 21–28.
19. F.J. Humphreys: *J. Mater. Sci.*, 2001, vol. 36, pp. 3833–54.
20. Z.Y. Chen, S.Q. Xu, and X.H. Dong: *Acta Metall. Sin. (Engl. Lett.),* 2008, vol. 21, pp. 451–58.
21. S. Liu, Q. Pan, H. Li, Z. Huang, K. Li, X. He, and X. Li: *J. Mater. Sci.*, 2019, vol. 54, pp. 4366–83.
22. S.F. Medina and C.A. Hernandez: *Acta Mater.*, 1996, vol. 44, pp. 137–48.
23. H. Mirzadeh, J.M. Cabrera, and A. Najafizadeh: *Acta Mater.*, 2011, vol. 59, pp. 6441–48.
24. H.J. McQueen, S. Yue, N.D. Ryan, and E. Fry: *J. Mater. Process. Technol.*, 1995, vol. 53, pp. 293–310.
25. Y.C. Lin and X.M. Chen: *Mater. Des.*, 2011, vol. 32, pp. 1733–59.
26. W. Liu, H. Zhao, D. Li, Z. Zhang, G. Huang, and Q. Liu: *Mater. Sci. Eng., A,* 2014, vol. 596, pp. 176–82.
27. C. Zener and J.H. Hollomon: *J. Appl. Phys.*, 1944, vol. 15, pp. 22–32.
28. Y. Dong, C. Zhang, G. Zhao, Y. Guan, A. Gao, and W. Sun: *Mater. Des.*, 2016, vol. 92, pp. 983–97.
29. H.R.R. Ashtiani and P. Shahsavari: *Mech. Mater.*, 2016, vol. 100, pp. 209–18.
30. J. Li, F. Li, J. Cai, R. Wang, Z. Yuan, and G. Ji: *Comput. Mater. Sci.*, 2013, vol. 71, pp. 56–65.
31. D.G. Eskin: *J. Mater. Sci.*, 2003, vol. 38, pp. 279–90.
32. J. Zhou, J. Duszczyk, B.M. Korevaar, and B. Verlinden: *J. Mater. Sci.*, 1992, vol. 27, pp. 4247–60.
33. H.E. Hu, X. Wang, and L. Deng: *Mater. Sci. Eng., A,* 2013, vol. 576, pp. 45–51.
34. N. Haghdadi, A. Zarei-Hanzaki, and H.R. Abedi: *Mater. Sci. Eng., A,* 2012, vol. 535, pp. 252–57.
35. M. Shakiba, N. Parson, and X.-G. Chen: *Mater. Sci. Eng., A,* 2015, vol. 636, pp. 572–81.
36. R. Le Gall and J.J. Jonas: *Acta Mater.*, 1999, vol. 47, pp. 4365–74.
37. H. Liao, Y. Wu, K. Zhou, and J. Yang: *Mater. Des.*, 2015, vol. 65, pp. 1091–99.
38. A.H. Feng, L. Geng, J. Zhang, and C.K. Yao: *Mater. Chem. Phys.*, 2003, vol. 82, pp. 618–21.
39. M. Huang, Z. Li, and J. Tong: *Int. J. Plast.*, 2014, vol. 61, pp. 112–27.
40. G. Neuman and C. Tuijn: *Self-diffusion and Impurity Diffusion in Pure Metals*, Pergamon, Amsterdam, 2008.
41. G. Meng, B. Li, H. Li, H. Huang, and Z. Nie: *Mater. Sci. Eng., A,* 2009, vol. 517, pp. 132–37.

42. S.K. Shaha, F. Czerwinski, W. Kasprzak, J. Friedman, and D.L. Chen: *J. Alloys Compd.*, 2014, vol. 615, pp. 1019–31.
43. Q. Yang, D. Yang, Z. Zhang, L. Cao, X. Wu, G. Huang, and Q. Liu: *Trans. Nonferrous Met. Soc. China*, 2016, vol. 26, pp. 649–57.
44. Q. Yang, X. Wang, X. Li, Z. Deng, Z. Jia, Z. Zhang, G. Huang, and Q. Liu: *Mater. Charact.*, 2017, vol. 131, pp. 500–507.
45. P.R. Thornton, T.E. Mitchell, and P.B. Hirsch: *Philos. Mag.*, 1962, vol. 7, pp. 1349–69.
46. D. Odoh, Y. Mahmoodkhani, and M. Wells: *Vacuum*, 2018, vol. 149, pp. 248–55.
47. R.C. Picu, G. Vincze, F. Ozturk, J.J. Gracio, F. Barlat, and A.M. Maniatty: *Mater. Sci. Eng., A,* 2005, vol. 390, pp. 334–43.
48. M.E. van Dalen, R.A. Karnesky, J.R. Cabotaje, D.C. Dunand, and D.N. Seidman: *Acta Mater.*, 2009, vol. 57, pp. 4081–89.
49. L.F. Mondolfo: *Aluminum Alloys: Structure and Properties*, Butterworths, Boston, MA, 1976.
50. X. Huang, H. Zhang, Y. Han, W. Wu, and J. Chen: *Mater. Sci. Eng., A,* 2010, vol. 527, pp. 485–90.
51. V.I. Yelagin and V.A. Livanov, eds.:*Structure and Properties of Semi-Finished Products from Aluminium Alloys*, Metallurgiya, Moscow, 1984, p. 28.